nature communications



Article

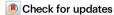
https://doi.org/10.1038/s41467-024-54204-2

Selective electrosynthesis of hydroxylamine from aqueous nitrate/nitrite by suppressing further reduction

Received: 12 March 2024

Accepted: 1 November 2024

Published online: 12 November 2024



Yirong Tang ® ^{1,4}, Zhan Jiang ® ^{1,2,4} ⋈, Yubo Yuan ® ^{1,4}, Li Xu³, Chuyao Jin³, Bulin Chen ® ¹, Zhichao Lin¹, Jie Zao¹, Jianwei Du², Xiao Zhang ® ³ ⋈, Xiang Gao ® ³ ⋈ & Yongye Liang ® ¹ ⋈

The electrocatalytic reduction of nitrogenous waste offers a sustainable approach to producing nitrogen-containing chemicals. The selective synthesis of high-value hydroxylamine (NH₂OH) is challenging due to the instability of NH₂OH as an intermediate. Here, we present a rational electrocatalyst design strategy for promoting NH₂OH electrosynthesis by suppressing the competing pathways of further reduction. We screen zinc phthalocyanines (ZnPc) with a high energy barrier for NH₂OH reduction by regulating their intrinsic activity. Additionally, we discover that carbon nanotube substrates exhibit significant NH₃-producing activity, which can be effectively inhibited by the high coverage of ZnPc molecules. In-situ characterizations reveal that NH₂OH and HNO are generated as intermediates in nitrate reduction to NH₃, and NH₂OH can be enriched in the ZnPc electrode. In the H-cell, the optimized ZnPc catalyst demonstrates a Faradaic efficiency (FE) of $53 \pm 1.7\%$ for NH₂OH with a partial current density exceeding 270 mA cm⁻² and a turnover frequency of $7.5 \pm 0.2 \,\mathrm{s}^{-1}$. It also enables the rapid electrosynthesis of cyclohexanone oxime from nitrite with a FE of $64 \pm 1.0\%$.

Electrocatalytic conversion technology offers a promising approach for the sustainable synthesis of high-value-added chemicals from environmental waste¹⁻⁹, such as carbon dioxide (CO₂), nitrate (NO₃⁻) and nitrite (NO₂⁻). This technology can be implemented under mild conditions using renewable energy sources, thus reducing the carbon footprint when compared to traditional methods. Achieving large current densities while maintaining high product selectivities is crucial in electrocatalytic technology, as it can drive cost reduction and enhance competitiveness^{10,11}. However, in the case of electrochemical reactions involving multi-electron and proton transfers, complex reaction pathways can lead to the formation of multiple products. Significantly, the selective production

of economically desirable intermediate products remains highly challenging^{12–16}.

Hydroxylamine (NH₂OH) is a valuable intermediate in electrocatalytic NO₃⁻ or NO₂⁻ reduction reactions (NO₃RR or NO₂RR). It is widely used in industries such as textiles, pharmaceuticals, semiconductors, and nuclear energy^{17,18}. The annual demand of NH₂OH worldwide is more than 10⁶ tons and NH₂OH is an important precursor for the synthesis of nylon-6 and other chemicals¹⁷. Today, NH₂OH is primarily produced via NH₃ oxidation to form nitrogen oxides (NO_x), followed by subsequent reduction with H₂ or SO₂^{19,20}. This intricate manufacturing process involves the use of explosive H₂ and corrosive SO₂ and NO_x, raising concerns about safety, cost, and sustainability²¹.

¹Department of Materials Science and Engineering, Southern University of Science and Technology, Shenzhen 518055, China. ²State Environmental Protection Key Laboratory of Water Environmental Simulation and Pollution Control, South China Institute of Environmental Sciences, Ministry of Ecology and Environment, Guangzhou 510655, China. ³State Key Laboratory of Clean Energy Utilization, State Environmental Protection Center for Coal-Fired Air Pollution Control, Zhejiang University Hangzhou 310027, China. ⁴These authors contributed equally: Yirong Tang, Zhan Jiang, Yubo Yuan.

e-mail: jiangz@sustech.edu.cn; zhangx_energy@zju.edu.cn; xgao1@zju.edu.cn; liangyy@sustech.edu.cn

Therefore, it is appealing to explore the sustainable production of NH₂OH using renewable electricity. NH₂OH is a minor by-product of electrocatalytic NO₃RR or NO₂RR to produce NH₃, and the reported NH₂OH partial current densities ($j_{\rm NH2OH}$) are currently two orders of magnitude lower than NH₃^{15,22-24}. For example, Guido et al. reported that a Ti hollow fiber electrocatalyst could achieve a $j_{\rm NH2OH}$ of 17 mA cm⁻² at -0.60 V vs. reversible hydrogen electrode (RHE) in 0.1 M HClO₄ with 50 mM KNO₃¹⁵ (Supplementary Fig. 1). In contrast, electrocatalysts promoting NH₃ formation have shown $j_{\rm NH3}$ nearly 1000 mA cm^{-2 II}. This significant difference may be ascribed to the intermediate nature of NH₂OH, as it is quite unstable and easily reduced to NH₃^{11,12,18,25,26}. Therefore, an electrocatalyst that can effectively stabilize NH₂OH intermediates from further reduction reaction (NH₂OHRR) is crucial for the selective production of NH₂OH.

In this study, we present a combined strategy that incorporates intrinsic activity tuning and external removal of side reaction sites to enable the selective electrochemical production of NH₂OH from NO₃⁻ or NO₂- (Fig. 1). We first tune the intrinsic performance of metal phthalocyanines (MPc) electrocatalysts by adjusting the metal center. Theoretical calculations and experimental results reveal that the ZnPc catalyst exhibits a higher energy barrier for NH2OH reduction, leading to higher NH₂OH FEs in NO₃RR. Furthermore, we discover the interference of the carbon nanotube (CNT) substrate as a side reaction site for NH₃ generation, and the higher coverage of ZnPc can eliminate this effect. We also use the in-situ characterization technique to monitor NO₃RR, showing that NH₂OH is generated as an intermediate and can be enriched in our system. The optimized ZnPc catalyst exhibits improved FE(NH₂OH)s even at high current densities, enabling rapid, selective, and stable in-situ electrosynthesis of cyclohexanone oxime from NO₃⁻ or NO₂⁻.

Results

Design and characterization of electrocatalysts

Molecular electrocatalysts have demonstrated high selectivity in various electrocatalytic reactions, as their well-defined structures enable precise control of reaction pathways through molecular design^{2,11,16,27,28}. In our previous study, the molecularly dispersed

electrocatalyst of cobalt β-tetraaminophthalocyanine (CoPc-NH₂ MDE) reduced NO₃⁻ to NH₂OH intermediate for the electrosynthesis of methylamine². However, the FE of NH₂OH through NO₃RR was lower than 5%. Guided by density functional theory (DFT) calculations, we initially predicted the electrocatalytic activity of MPcs with different metal centers (M = Co. Fe. and Zn) in NH₂OHRR (Fig. 2a. b). The free energy diagrams show that the NH₂OHRR process first encounters an energy barrier during NH₂OH adsorption (NH₂OH to *NH₂OH), followed by several free energy downhill processes. The NH2OH adsorption energy barrier for CoPc is only 0.09 eV, facilitating the further reduction of NH₂OH. Conversely, ZnPc and FePc exhibit higher NH₂OH adsorption energy barriers than CoPc, and ZnPc displays the highest NH₂OH adsorption energy barrier of 0.49 eV. This indicates that ZnPc has significantly lower activity in catalyzing NH₂OHRR, suggesting it may be a more selective candidate for NH₂OH production in NO₃RR.

MPcs easily aggregate when directly deposited on the electrode surface^{11,27-29}. On the surface of the ZnPc aggregated electrocatalyst (AE) working electrode, significant aggregate particles with size ranging from 0.2 to 20 µm could be observed by scanning electron microscopy (SEM) (Fig. 2c and Supplementary Fig. 2). This aggregation would slow down the transfer of electrons from the electrode to surface active sites, often resulting in poor catalytic performance^{27–29}. To address this issue, we anchored the molecules on the surface of multiwalled carbon nanotubes (CNTs) through π - π interactions and prepared MPc MDEs, which can enhance the exposure of active sites and accelerate the catalysis, enabling the studies of the real electrocatalytic performance of MPc. From the SEM and transmission electron microscope (TEM) images, aggregation of MPc molecules was prevented in MDEs (Fig. 2d, e and Supplementary Fig. 3). On the surface of CNTs, MPcs appear to be in a molecularly dispersed state, as indicated by the isolated bright spot in the high-angle angular dark-field scanning transmission electron microscopy (HAADF-STEM) figure (Fig. 2e). Zn 2p X-ray photoelectron spectroscopy (XPS) further confirmed that the metal center of MPc in MDEs maintain its original valence state, as there is no obvious shift in binding energy (Supplementary Fig. 4). The metal content in the MPc MDEs was controlled to be around 0.3 wt.%.

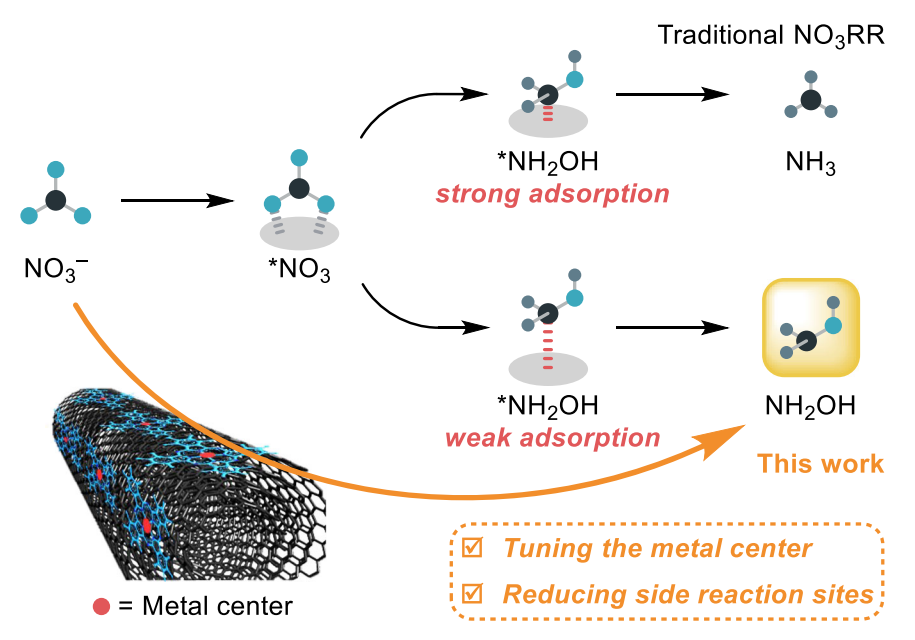


Fig. 1 | Selective production of NH₂OH from nitrate by metal phthalocyanine electrocatalysts. The schematic diagram shows the tuning of the nitrate reduction reaction for selective NH₂OH production on the molecularly dispersed electrocatalysts (MDEs) of metal phthalocyanine (MPc) supported on CNTs. The deep blue

moieties represent the MPc molecules, and the black material represents the CNT substrate. The deep green, pale blue, and grey balls represent the N, O, and H atoms. The ellipse substrates represent the active sites on the electrocatalyst.

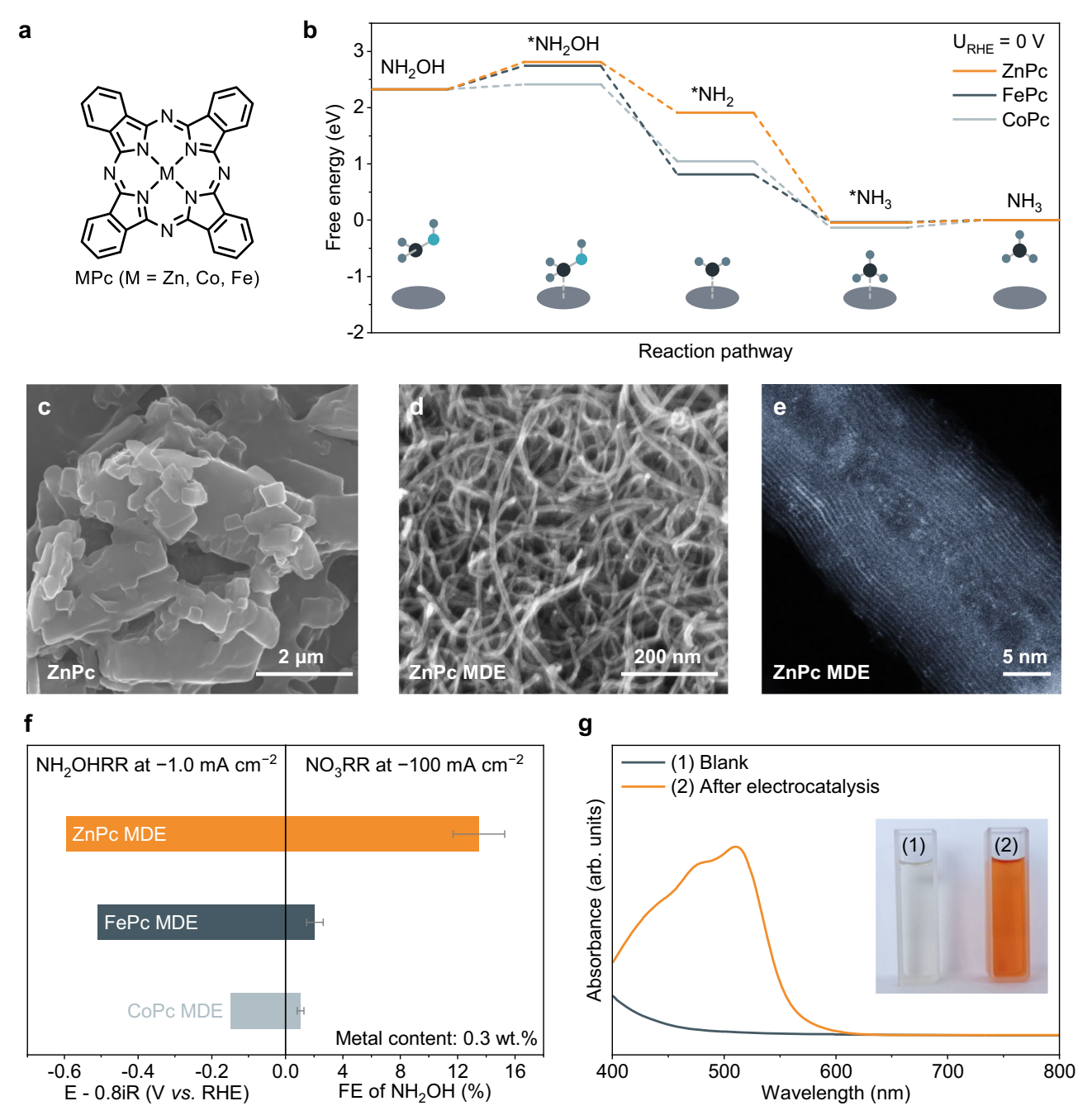


Fig. 2 | DFT calculations and electrocatalytic performance of MPc MDEs. a The molecular structure of MPc, M refers to the metal center. b The free energy diagram for NH $_2$ OHRR on various MPcs at 0 V vs. RHE. The ellipse substrates represent the active sites on the electrocatalyst. The black, blue and grey balls represent the N, O and H atoms, respectively. c SEM image of ZnPc aggregated electrocatalyst (AE). d SEM image of ZnPc MDE. e HAADF-STEM image of ZnPc MDE. The bright spots correspond to the Zn center of ZnPc. f The electrocatalytic performances of MPc MDEs. The left side illustrates the required potentials in NH $_2$ OHRR to achieve a current density of -1.0 mA cm $^{-2}$ in an electrolyte of 1.0 M KOH containing 33 mM

NH $_2$ OH (150 mL), R $_u$ = 10.0 ± 3.4 Ω . The right side displays their FE(NH $_2$ OH) in NO $_3$ RR at a current density of –100 mA cm $^{-2}$ in an electrolyte of 1.0 M KOH+1.0 M KNO $_3$ (14 mL), R $_u$ of CoPc, FePc and ZnPc MDE are 5.5 ± 0.1 Ω , 4.4 ± 0.1 Ω and 4.7 ± 0.4 Ω . The metal content: - 0.3 wt.%. Three individual measurements were taken with various working electrodes, and the average (mean) values are presented with the standard deviation as error bars. **g** UV–Vis spectra of colorimetric quantification of NH $_2$ OH. The orange color shows the presentation of NH $_2$ OH in solution, which can reduce Fe $^{3+}$ to Fe $^{2+}$, forming an orange complex with 1,10-phenanthroline. The abbreviation "arb. units" refers to "arbitrary units".

The linear scanning sweep voltammetry (LSV) curves for NH_2OHRR tests were conducted in a 1.0 M KOH electrolyte containing 33 mM NH_2OH (Supplementary Fig. 5). All potentials were converted to versus RHE. To achieve a NH_2OHRR current density of -1.0 mA cm⁻², ZnPc MDE exhibits the highest potential requirement of -0.60 V, which was 450 mV more negative than CoPc MDE (Fig. 2f). Thus, ZnPc MDE is the least active catalyst for NH_2OHRR , followed by FePc and CoPc, consistent with the theoretical calculation.

NO₃RR performance of ZnPc MDEs

The electrocatalytic NO_3RR performances were tested in a $1.0\,M$ KOH + $1.0\,M$ KNO₃ electrolyte (Fig. 2f and Supplementary Fig. 6). Gaseous products, mainly hydrogen (H₂), were detected using gas chromatography (Supplementary Fig. 7). Liquid products, primarily consisting of NO_2 , NH_2OH , and NH_3 , were identified using colorimetric methods and ultraviolet-visible (UV–Vis) spectrophotometry (Supplementary Figs. 8–10)³⁰. In addition, the accuracy of the

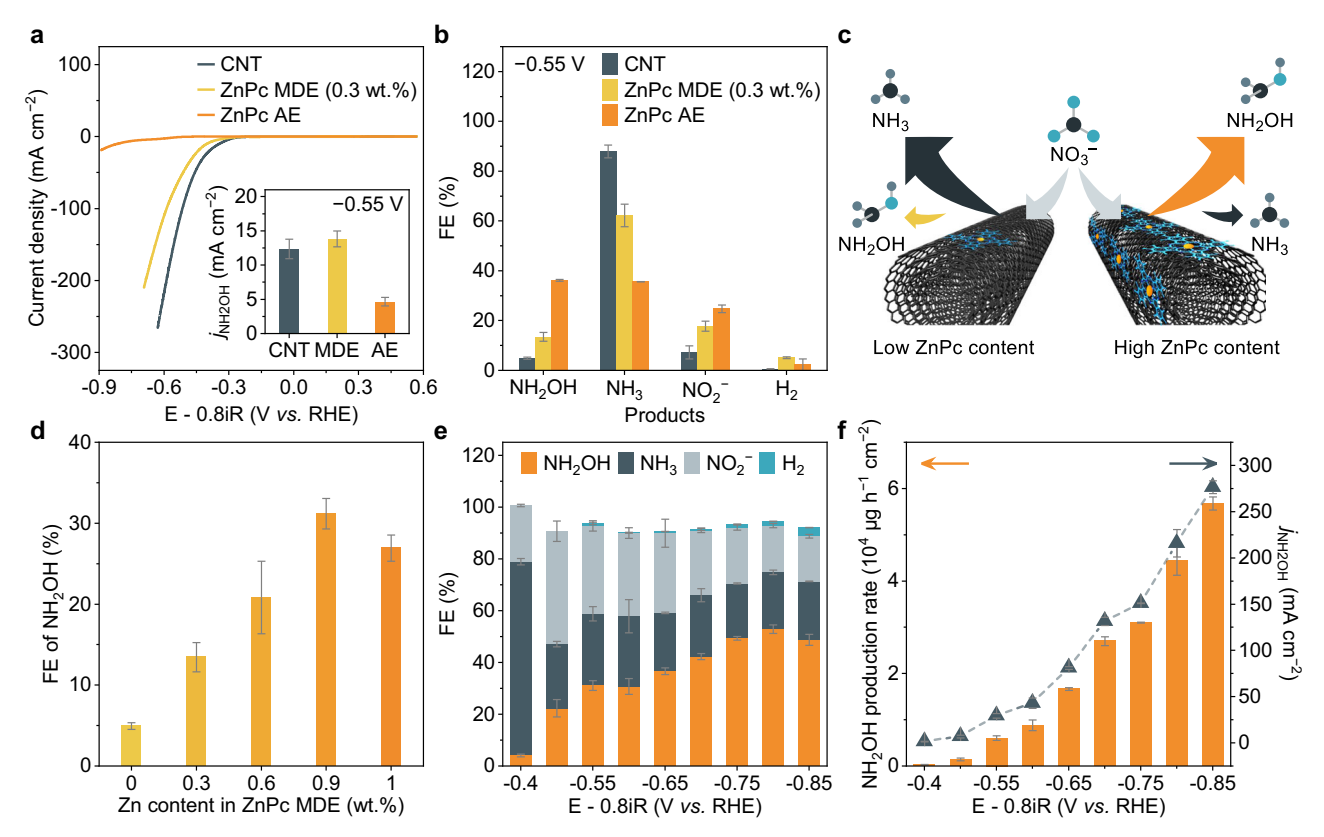


Fig. 3 | **Electrocatalytic performance of ZnPc MDE for NO**₃**RR. a** LSV curves of NO₃RR performance with bare CNT, ZnPc MDE, and ZnPc AE. Scan rate, 20 mV s⁻¹. The inset shows their j_{NH2OH} at -0.55 V. R_{u} of CNT, ZnPc MDE and ZnPc AE are $4.9 \pm 0.3~\Omega$, $4.8 \pm 0.1~\Omega$, and $6.1 \pm 0.8~\Omega$. **b** The FE values of various NO₃RR products at the applied potential of -0.55 V. **c** Schematic diagram shows the variation of the NO₃RR pathway on ZnPc MDE with different ZnPc loadings. The black ball represents the N atom, the pale blue ball represents the O atom, and the grey ball represents the H atom. The black items with hexagonal structures represent the CNT substrate, and the items with light blue molecular structure and orange center

represent the ZnPc molecules. **d** FE(NH₂OH)s for NO₃RR by ZnPc MDE with varying Zn contents at -0.55 V. R_u of ZnPc MDE with metal content of 0, 0.3, 0.6 and 0.9 wt.% are $4.9 \pm 0.3 \ \Omega$, $4.8 \pm 0.1 \ \Omega$, $4.4 \pm 0.1 \ \Omega$, and $4.3 \pm 0.2 \ \Omega$. **e** The FE values of various NO₃RR products at different applied potentials by ZnPc MDE(H). **f** The NH₂OH production rate and j_{NH2OH} at different applied potentials by ZnPc MDE(H). All electrocatalysis measurements were conducted in an Ar-protected 1.0 M KOH + 1.0 M KNO₃ electrolyte. Three individual measurements were taken with various working electrodes, and the average (mean) values are presented with the standard deviation as error bars.

colorimetric quantification of NH₂OH was verified by the Nuclear Magnetic Resonance (NMR) method (Supplementary Fig. 11), and the influence of different N-containing species was also investigated (Supplementary Fig. 12). After the electrocatalysis, the solution containing a high concentration of NH₂OH molecules displayed a vibrant orange color (Fig. 2g). After a 30-min constant current test at $-100~\text{mA}~\text{cm}^{-2}$, the ZnPc MDE delivered the highest FE(NH₂OH) of $14\pm1.8\%$, followed by FePc MDE. The CoPc MDE exhibits a FE(NH₂OH) of only $1.0\pm0.2\%$, which is 10 times lower than that of ZnPc MDE. These findings indicate that it is possible to design catalysts that selectively produce NH₂OH by investigating catalysts with low inherent performance in NH₂OHRR.

The performance of the ZnPc AE and ZnPc MDE in NO $_3$ RR was compared (Fig. 3a, b). From the LSV curves, it is evident that ZnPc AE exhibits a much lower reduction current density in NO $_3$ RR than ZnPc MDE (Fig. 3a). However, the FE(NH $_2$ OH) of ZnPc AE was significantly higher than that of ZnPc MDE. At a potential of -0.55 V, FE(NH $_2$ OH) of ZnPc AE was as high as $36 \pm 0.4\%$, while ZnPc MDE was only $14 \pm 1.8\%$. This indicates that ZnPc molecules play a central role in ZnPc MDE for NH $_2$ OH production in NO $_3$ RR (Fig. 3b). Despite exhibiting high NH $_2$ OH selectivity, ZnPc AE shows lower electrocatalytic activity than ZnPc MDE. For example, the $j_{\text{NH}2OH}$ of ZnPc AE was only 4.7 ± 0.6 mA cm $^{-2}$ at -0.55 V, which is approximately one-third of that of ZnPc MDE (Fig. 3a). Therefore, introducing CNT with high conductivity is beneficial for enhancing the electrocatalytic activity of ZnPc in the production of NH $_2$ OH.

Interestingly, we noticed that FE(NH₃) of ZnPc MDE was significantly higher than that of ZnPc AE, with values of $62\pm4.5\%$ and $36\pm0.1\%$ respectively (Fig. 3b). This suggests the presence of more favorable catalytic sites for NH₃ production in ZnPc MDE compared to ZnPc AE. Therefore, we investigated the performance of the CNT substrate in NO₃RR. Unlike traditional substrates, which are often less active^{29,31}, bare CNTs here exhibit significantly higher NO₃RR activity than ZnPc MDE (Fig. 3a). We also find that bare CNTs favor the production of NH₃, with a FE(NH₃) as high as $88\pm2.6\%$ at -0.55 V (Fig. 3b). These findings demonstrate that there are side reaction sites on bare CNTs that compete with ZnPc molecules in ZnPc MDE (Fig. 3c) for NO₃RR. Thus, a viable strategy to enhance the NH₂OH selectivity is to block the side reaction center by coating the surface of CNTs with a sufficient amount of ZnPc molecules.

To validate this assumption, we further investigated the impact of ZnPc content in ZnPc MDE on the FE(NH₂OH) in NO₃RR at a potential of $-0.55\,V$ (Fig. 3d). As the Zn content increases from 0 to 0.9 wt.%, FE(NH₂OH) is significantly enhanced (Fig. 3d) and reaches 31 \pm 1.9% at a Zn content of 0.9 wt.%, which is similar to the FE(NH₂OH) of ZnPc AE (36 \pm 0.4%). In contrast, FE(NH₃) gradually decreases as the Zn content increases (Supplementary Fig. 13). These results suggest that increasing the coverage of ZnPc on CNTs effectively enhances the selective reduction of NO₃ $^-$ to NH₂OH. It is also found that the further increase of Zn content results in a slight decrease of FE(NH₂OH), possibly due to the overloading of ZnPc molecules on CNTs (Fig. 3d, Supplementary Fig. 13 and 14).

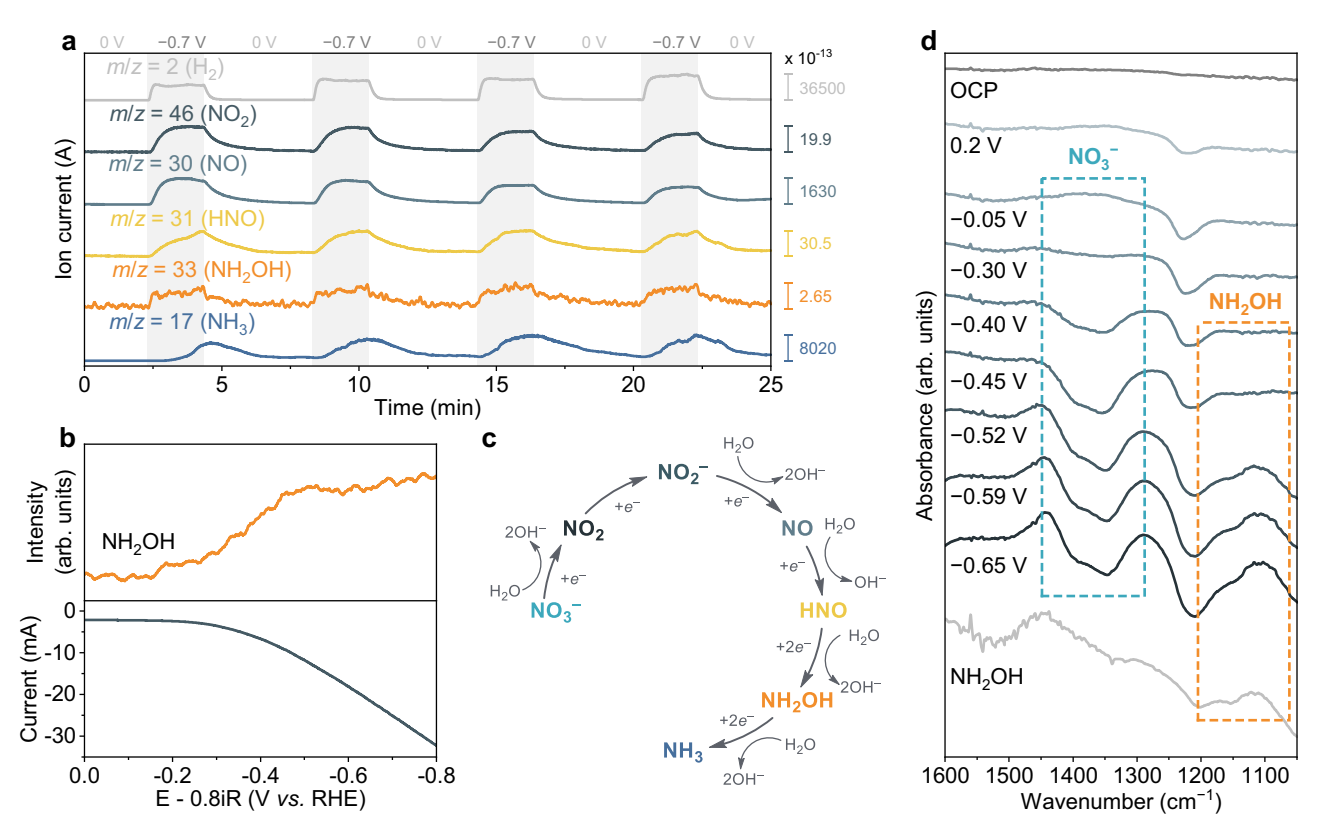


Fig. 4 | **In-situ DEMS and ATR-FTIR characterization of electrocatalytic NO**₃RR **on ZnPc MDE(H). a** In-situ DEMS measurements for electrocatalytic NO₃RR at -0.7 V over four continuous cycles. The mass signals increased rapidly upon application of the reduced potential and gradually decreased to the baseline after the potential was removed. **b** In-situ DEMS of NH₂OH changes with applied potential in LSV. Scan rate of LSV: 1.0 mV s⁻¹. The abbreviation "arb. units" refers to "arbitrary units". $R_u = 12.9 \pm 1.1$ Ω . **c** The electrocatalytic NO₃RR pathway in our experiment, derived from our in-situ DEMS experiment results. **d** In-situ ATR-FTIR

spectra of the electrocatalytic NO_3RR . As the spectra were background corrected, the downward peak change in the blue region indicates the consumption of NO_3^- , and the upward peak change in the yellow region signifies the formation of NH_2OH . R_u = $11.1 \pm 0.1~\Omega$. All in-situ characterization experiments were conducted in an Arsaturated 1.0 M KOH + 1.0 M KNO $_3$ electrolyte. Resistances were measured by three individual measurements, and the average (mean) values with the standard deviation are presented.

The NO₃RR performance of the high ZnPc coverage MDE with the Zn content of 0.9 wt.%, marked as ZnPc MDE(H), was further investigated at various potentials (Fig. 3e). NH₂OH can be detected at -0.50 V with a FE(NH₂OH) of $22 \pm 3.3\%$. In the range of -0.70 to -0.85 V, FE(NH₂OH)s exceeds 40%. Specifically, we achieve the highest FE(NH₂OH) of $53 \pm 1.7\%$ at the potential of -0.80 V. The highest j_{NH2OH} reaches $277 \pm 7.0 \,\mathrm{mA \, cm^{-2}}$ at the potential of $-0.85 \,\mathrm{V}$, equivalent to a production rate of 57 ± 1.4 mg h⁻¹ cm⁻² (Fig. 3f). The NH₂OH-production turnover frequency (TOF) of the ZnPc MDE(H) is calculated to be $7.5 \pm 0.2 \,\mathrm{s}^{-1}$ (based on the number of electrochemically active ZnPc molecules determined from cyclic voltammetry, 63 nmol cm⁻², Supplementary Fig. 15). This performance is significantly superior to that of recently reported electrocatalysts for NO₃RR to NH₂OH, such as Ti hollow fiber¹⁵, which achieved a FE(NH₂OH) of 27% and j_{NH2OH} of 24 mA cm⁻² (Supplementary Fig. 1). It is important to note that FE(NH₃) is not over ~25% even at a more negative potential of -0.85 V for ZnPc MDE(H), highlighting the efficacy of high ZnPc coverage in inhibiting the NH₂OHRR process (Fig. 3e).

Mechanistic insights for NH₂OH production in NO₃RR

To gain insights into the NH₂OH generation mechanism on ZnPc MDE(H), in-situ differential electrochemical mass spectrometry (DEMS) was employed to analyze intermediates during NO₃RR in $1.0 \,\mathrm{M}$ KOH + $1.0 \,\mathrm{M}$ KNO₃ (Fig. 4a, b). In the multi-potential steps test, the mass-to-charge-ratios (m/z) of 2, 46, 30, 31, 33, and 17 were recorded, corresponding to H₂, NO₂, NO, HNO, NH₂OH, and NH₃, respectively (Fig. 4a, Supplementary Fig. 16). The clear detection of

intermediates, such as NO, HNO, and particularly NH_2OH , can be ascribed to the high selectivity of ZnPc MDE(H)s in producing NH_2OH . We then further investigated potential-dependent NH_2OH DEMS measurements. NH_2OH can be detected below $-0.15\,V$, suggesting it is a key intermediate in NO_3RR (Fig. 4b). Additionally, we performed the same multi-potential steps test using isotopically labeled $K^{15}NO_3$ (Supplementary Fig. 17). Significant signals corresponding to $^{15}NO_2$ (m/z=47), ^{15}NO (m/z=31), $^{15}NH_2OH$ (m/z=34), and $^{15}NH_3$ (m/z=18) were detected, confirming that these intermediates are produced from NO_3RR . We also performed the electrocatalytic NO reduction on ZnPc MDE(H) (Supplementary Fig. 18). The electrocatalyst exhibits apparent NO reduction activity in 1.0 M KOH, and NH_2OH is detected after a 30-min electrolysis at $-0.80\,V$ vs. RHE. Thus, the NO_3RR by the ZnPc MDE(H) proceeds in the following reaction pathway: $NO_3^- \rightarrow NO_2^- \rightarrow NO \rightarrow HNO \rightarrow NH_2OH \rightarrow NH_3$ (Fig. 4c).

In addition, we also performed potential-dependent in-situ attenuated total reflection Fourier transform infrared spectroscopy (ATR-FTIR) analysis with the potential dependency (Fig. 4d). Two distinct troughs were observed at 1350 and 1398 cm⁻¹ appeared at a potential of $-0.30\,\mathrm{V}$ and their prominence increased at more negative potentials, indicating the depletion of NO_3^- near the electrode surface^{22,32}. Meanwhile, two peaks in the range of 1100 to 1200 cm⁻¹ are associated with the N-O stretching of the formed NH₂OH³², which is corroborated by the direct addition of NH₂OH to the electrolyte prior to electrocatalysis. The emergence of the surface NH₂OH peak signal immediately follows the consumption of NO_3^- at $-0.4\,\mathrm{V}$, indicating that NH₂OH is produced as a result of the NO₃RR. As the potential becomes

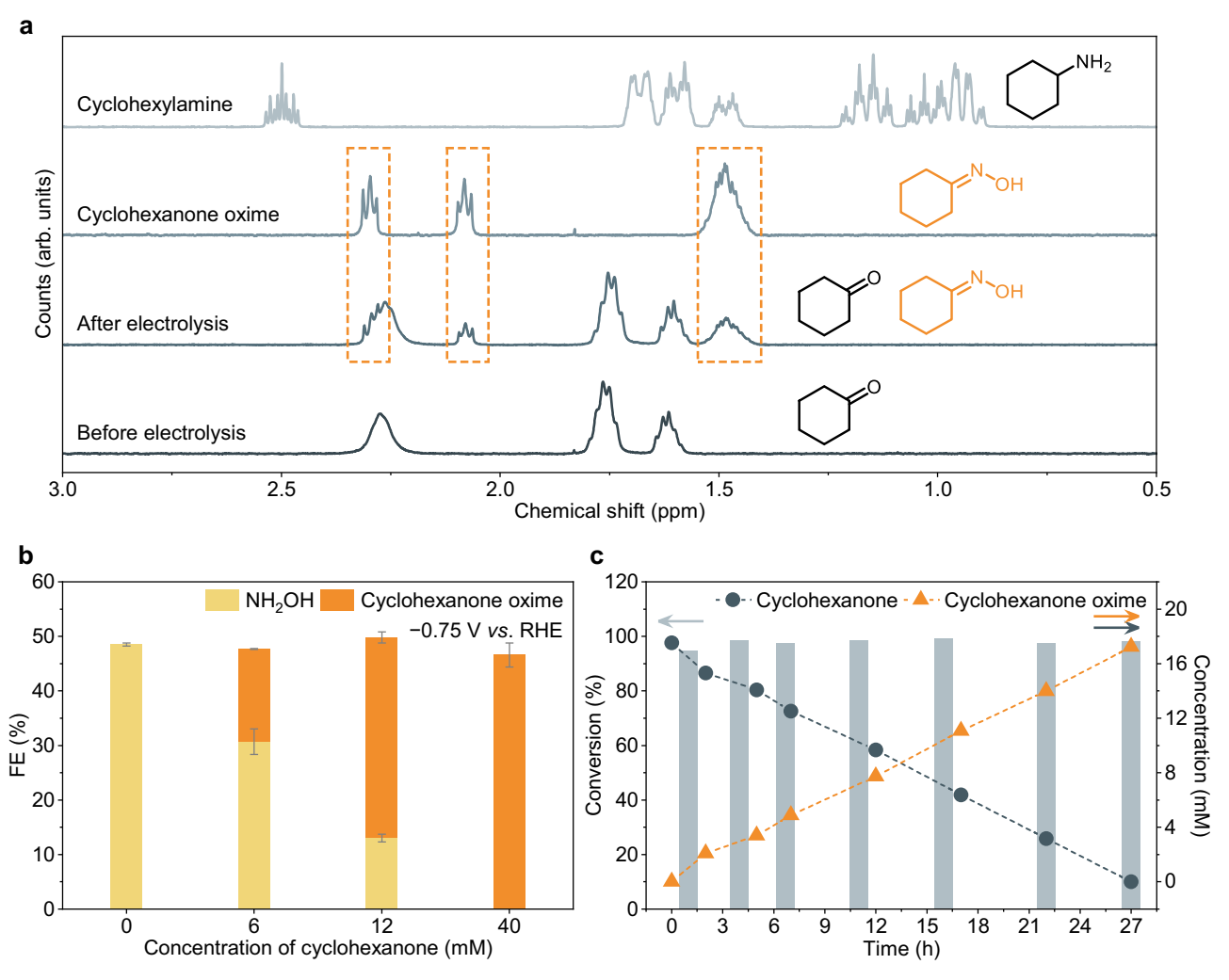


Fig. 5 | The NO $_3$ RR performance of ZnPc MDE(H) for the electrosynthesis of cyclohexanone oxime. a 1 H-NMR spectra of standard cyclohexanone (CYC), standard cyclohexanone oxime, electrolytes after electrocatalysis, and electrolytes before electrocatalysis containing 1.0 M KOH + 1.0 M KNO $_3$ with 6 mM CYC. The yellow boxes indicate the detection of distinct peaks of cyclohexanone oxime in the electrolyte following catalysis, with no other distinctive peaks of side products such as cyclohexylamine. The abbreviation "arb. units" refers to "arbitrary units". b NH $_2$ OH and cyclohexanone oxime formation FE on ZnPc MDE(H) in NO $_3$ RR with varying concentrations of CYC in 1.0 M KOH + 1.0 M KNO $_3$ electrolytes at an

applied potential of -0.75 V. R_u of ZnPc MDE(H) in the electrolyte with 0, 6, 12 and 40 mM of CYC were $5.2\pm0.2~\Omega$, $5.6\pm0.1~\Omega$, $5.7\pm0.1~\Omega$ and $6.0\pm0.2~\Omega$. Three individual measurements were taken with various working electrodes, and the average (mean) values are presented with the standard deviation as error bars. c Long-term electrosynthesis for a large amount of cyclohexanone oxime. The bars represent the conversion rate of CYC, and the symbols represent the concentration of CYC or cyclohexanone oxime in the electrolyte. Tested in a flow cell with a constant current of 250 mA using 0.5 L of electrolyte (1.0 M KOH + 1.0 M KNO₃, 40 mM CYC), R_u = 1.2 Ω .

more negative, these two peaks steadily increase to a highly significant signal level. This trend exhibits a robust and consistent correlation with the electrochemical measurements (Fig. 3) and in-situ DEMS results (Fig. 4b). The trough at 1217 cm⁻¹ is ascribed to the Si-O-Si bond of the substrate^{33,34}. The prominent signal of NH₂OH observed in ATR-FTIR spectroscopy offers compelling evidence that NH₂OH is enriched in the electrolyte as the major product produced by ZnPc MDE(H) during NO₃RR.

Electrosynthesis of cyclohexanone oxime

Recently, it has been demonstrated that higher-value chemicals, such as methylamine², cyclohexanone oxime^{4,5}, and amino acids³³, can be produced from the in situ formed NH₂OH. Among them, cyclohexanone oxime is an essential precursor in synthesizing high-performance polymers like nylon^{4,5}. Consequently, we further investigated the performance of ZnPc MDE(H) for the selective electrosynthesis of cyclohexanone oxime by reacting cyclohexanone (CYC) with NH₂OH produced in situ.

The synthesis of cyclohexanone oxime by ZnPc MDE(H) was performed in a 1.0 M KNO₃ + 1.0 M KOH solution containing CYC. The successful synthesis of cyclohexanone oxime is confirmed by analyzing ¹H-NMR spectroscopy for the electrolyte after the reaction (Fig. 5a and Supplementary Fig. 19). It is noteworthy that ZnPc MDE(H) demonstrates a high selectivity of 100% in the electrochemical conversion of ketones to oximes, without any detectable by-products such as cyclohexanol or cyclohexylamine. In addition, ZnPc MDE(H) does not show an increase of reduction current densities with the addition of 40 mM cyclohexanone or cyclohexanone oxime, which suggests the difficulty of reducing CYC or cyclohexanone oxime by ZnPc electrocatalysts (Supplementary Fig. 20) These highlight the unique advantages of ZnPc MDE(H), including efficient use of raw materials and no side reaction products. The notable performance of ZnPc MDE(H) surpasses the reported Fe⁵ and Pd³⁵ catalysts, which produce cyclohexanol as a byproduct through cyclohexanone reduction, as well as OD-Ag³³ and CoPc-NH₂ MDE², which produce cyclohexylamine as a byproduct through oxime reduction.

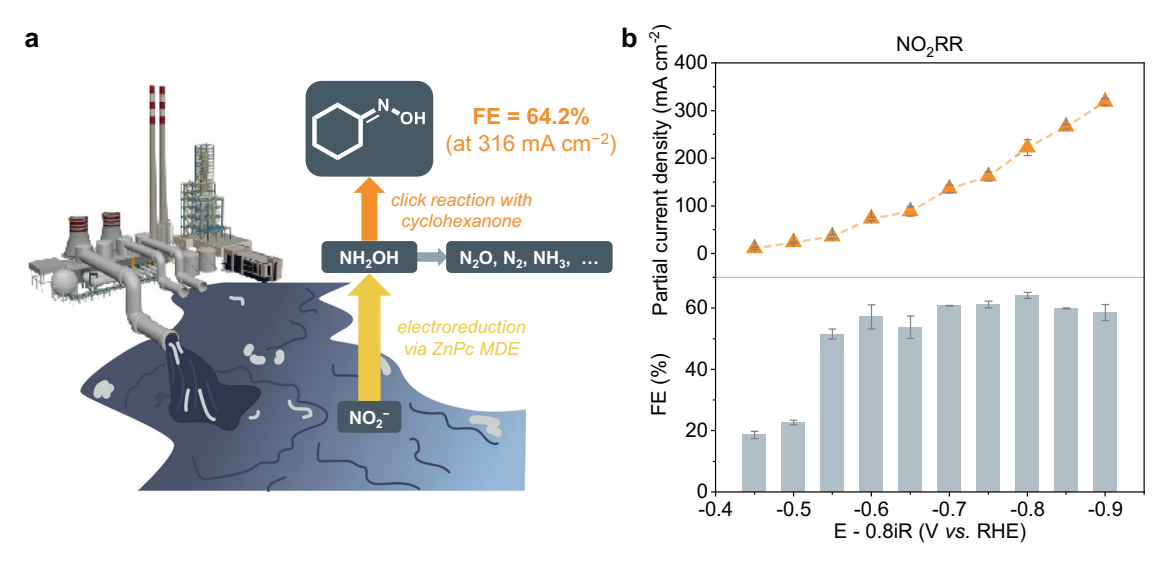


Fig. 6 | The NO $_2$ RR performance of ZnPc MDE(H) for the electrosynthesis of cyclohexanone oxime. a Schematic of the electrosynthesis of cyclohexanone oxime in the NO $_2$ RR with CYC. **b** FE of cyclohexanone oxime (bottom) and NH $_2$ OH partial current density (top) at various potentials in an Ar-protected 1.0 M KOH +

 $1.0\,\text{M KNO}_2$ + $40\,\text{mM}$ CYC electrolyte. R_u = $6.3\pm0.4\,\Omega$. Three individual measurements were taken with various working electrodes, and the average (mean) values are presented with the standard deviation as error bars.

The impact of CYC concentration on the synthesis of cyclohexanone oxime was further investigated at -0.75 V (Fig. 5b and Supplementary Fig. 21). At a CYC concentration of 6.0 mM in the electrolyte, the FE of cyclohexanone oxime is $17 \pm 0.1\%$, and no unreacted CYC is detected. NH₂OH is still detectable in the solution with an FE of $31 \pm 2.3\%$, indicating that ZnPc MDE(H) can convert CYC to cyclohexanone oxime with 100% efficiency when there is sufficient NH₂OH generation. As the concentration of CYC in the electrolyte increased, there is a gradual decrease in the NH₂OH content in the reacted electrolyte, accompanied by a corresponding increase in the content of cyclohexanone oxime. At a CYC concentration of 40 mM, the maximum FE of cyclohexanone oxime reaches a peak of $47 \pm 2.2\%$. This FE value is twice as significant as that of the previously reported Fe⁵ catalyst for the production of cyclohexanone oxime from NO₃RR with a CYC concentration of 0.1 M. NH₂OH is no longer detectable in the electrolyte after the reaction, while unreacted CYC remains. It is important to note that the increase of CYC concentration does not significantly improve the overall FEs of NH₂OH + cyclohexanone oxime (Fig. 5b). This suggests that CYC in our system does not substantially stabilize NO₃RR at the *NH₂OH step, different from other catalysts reported for the electrosynthesis of cyclohexanone oxime. The feature of ZnPc MDE(H) enables the selective electrosynthesis of cyclohexanone oxime at low CYC concentrations. This discovery offers additional evidence supporting the preferred generation of NH₂OH on the ZnPc catalyst and its stability in the electrolyte.

Interestingly, FE(NH $_2$ OH) declines in an electrolyte without CYC as time extends while the FE of oxime remains stable in an electrolyte with 40 mM CYC. The difference is ascribed to the fast conversion of NH $_2$ OH to cyclohexanone oxime and no accumulation of NH $_2$ OH in the electrolyte (Supplementary Figs. 22 and 23). We further investigated the electrocatalytic performance of ZnPc MDE(H) for the prolonged conversion of CYC to cyclohexanone oxime in larger amounts using a flow cell (Fig. 5c). Over a continuous 27-hour operation period with a current of 250 mA, 2 g of CYC (in 0.5 L 1.0 M KOH + 1.0 M KNO $_3$, 40 mM) is successfully converted to cyclohexanone oxime completely, exhibiting an average FE of 42% for cyclohexanone oxime. The XPS spectra analysis confirms that ZnPc in ZnPc MDE(H) remained unchanged after the long-term operation,

suggesting the excellent stability of ZnPc MDE(H) (Supplementary Fig. 24).

We noticed that the FE of NO₂⁻ as an intermediate product constitutes about 17% to the FE on the ZnPc MDE(H)-catalyzed NO₃RR (Fig. 3e). This implies that substituting KNO₃ with KNO₂ as the reactant may further improve the selectivity of NH₂OH production. Moreover, employing CYC as a capture agent for the produced NH₂OH may hinder its rapid decomposition in the KNO₂ electrolyte (Fig. 6a and Supplementary Fig. 23). In light of this, we performed NO₂RR tests in an H-cell using an electrolyte of 1.0 M KOH + 1.0 M KNO₂ containing with 40 mM CYC. At the same potentials, FEs of cyclohexanone oxime in the NO₂RR are significantly higher than the FE(NH₂OH) in the NO₃RR (Fig. 6b). Within the wide potential range from -0.55 V to -0.90 V, FE of cyclohexanone oxime exceeds 50% and reached its peak of $64 \pm 1.0\%$ at -0.80 V. The partial current density of cyclohexanone oxime reaches as high as 318 ± 6.9 mA cm⁻² at -0.90 V. This performance surpasses that of other reported electrocatalysts, such as Cu-S4, which exhibited a cyclohexanone oxime FE of 27% and a partial current density of 18 mA cm⁻² (Supplementary Fig. 1).

Discussion

In this study, a de novo electrocatalyst design strategy has been developed for rapid and selective NH₂OH production from NO₃RR or NO₂RR. ZnPc with a high energy barrier for NH₂OHRR can thermodynamically suppress the further reduction of NH₂OH to NH₃. The blocking of side reaction centers on the CNT substrate by high coverage of ZnPc can inhibit the side reaction pathway from NO₃⁻ to NH₃. With these features, the optimized ZnPc MDE(H) exhibits impressive FE(NH₂OH)s of over 50% even at high current densities up to 410 mA cm⁻². The produced NH₂OH also enables highly selective electrosynthesis of cyclohexanone oxime at low CYC concentrations, exhibiting an FE of 64% and partial current densities exceeding 318 mA cm⁻² in NO₂RR. In-situ characterizations clearly reveal that NH₂OH and HNO are intermediates during nitrate electroreduction, and confirm the enrichment of NH₂OH on the ZnPc MDE-modified electrode. This study also provides a guiding principle for electrocatalyst design in the electrosynthesis of high-value intermediate chemicals.

Methods

Preparation of MPc MDEs

MPc MDEs were prepared using a reported method²⁷. Take the preparation of ZnPc MDE(H) as an example. At first, as-received CNTs (FT9100, C-Nano) were calcined at 500 °C in air for 5 h. After cooling to room temperature, they were sonicated in the 5 wt.% HCl (Dongijang Chemical Reagent) solution for 30 mins. The purified CNTs were collected after filtration, washing by deionized water and drying. 30 mg of purified CNTs were dispersed in 15 ml of N, N-Dimethylformamide (DMF, ≥ 99.5%, General-Reagent from Titan Co. Ltd) with the help of ultrasound for 1 hour. 3.75 mg of ZnPc (97%, Sigma-Aldrich) dispersed in 15 ml of DMF was mixed with the CNT dispersion, followed by sonication for another 1 hour. After 24 h stirring, ZnPc MDE(H) was finally obtained through centrifugation, followed by two ethanol (≥ 99.7%, Energy Chemical) washes, two deionized water washes, and freeze-drying. The preparation of other MPc MDEs is the same as above but in various ratio or with different MPc molecules, like FePc (96%, Alfa Aesar) and CoPc (Alfa Aesar). Deionized water used throughout all experiments was purified through either a Pall or a Millipore water purification system to reach a resistivity of 18.2 M Ω ·cm (at 25 °C).

Characterization

Shimadzu UV-Vis spectrophotometer 3600 was used for UV-Vis absorption measurements. ICP-MS was performed with Agilent Technologies 7700X. ^1H NMR was recorded on a Bruker 400 M NMR instrument. XPS was conducted on a Thermo Fisher Escalab Xi+instrument with Al K α radiation resource. SEM images were taken from Hitachi ultra-high resolution SEM Regulus 8230. STEM image was taken from Thermo Fisher (formerly FEI) Titan Themis G2 200 Probe Cs Corrected STEM. In-situ FTIR spectra were collected using a Nicolet iS50 FTIR spectrometer from Thermo Fisher. In-situ DEMS data was collected using a QAS 100 mass spectrometer from Linglu Instruments (Shanghai) Co. Ltd.

Electrochemical measurements

All electrochemical measurements were measured in a three-electrode configuration with a CHI 660E potentiostat (Counter electrode: platinum plate (99.99%, Gaoss Union); reference electrode: saturated calomel electrode (Gaoss Union)) and at 25 °C unless stated otherwise. All potentials were converted to versus RHE with 80% *iR* corrections³⁶ by using the following equation:

$$E_{RHE} = E_{SCE} + 0.240 + 0.0591 \times pH - 80\% iR_u$$
 (1)

where E_{SCE} is measured working potential corresponding to the reference electrode, i is the average current, and R_u is the solution resistance and measured by the iR compensation method in potentiostat.

The NH₂OHRR tests of MPc MDE were conducted on a rotating disk electrode (RDE). The electrolyte was Ar-protected 1.0 M KOH + 33 mM NH₂OH. KOH (ACS) was purchased from Aladdin and hydroxylamine hydrochloride (NH₂OH·HCl, 99%+) was from Adamas beta. The working electrodes were prepared by dropping 20 μ l catalyst ink of MPc MDE (2 mg of catalyst in 2 ml of ethanol containing 13 μ l of 5 wt.% Nafion solution (Dupont)) onto glassy carbon RDE (Gaoss Union) of 5 mm in diameter giving a loading of 0.1 mg cm $^{-2}$. The rotation speed was fixed at 1600 rpm. Ar (99.999%, Huashidai Gas) was bubbled into the electrolyte solution (100 sccm) during the test.

The NO_3RR tests were performed in a homemade H-cell (Supplementary Fig. 25) with Ar-protected 1.0 M KOH + 1.0 M KNO₃, with pH = 14.03 ± 0.02 (mean \pm s.d., three individual measurements were taken). The working electrodes were prepared by drop-casting $200 \,\mu$ l of catalyst inks on carbon paper (Toray 030, 30% PTFE-treated, Fuel Cell Store) to get a catalyst mass loading of $0.4 \,\mathrm{mg}\,\mathrm{cm}^{-2}$ with an electrode area of $0.5 \,\mathrm{cm}^2$. During the test, electrolyte in the

cathode compartment was stirred at 300 rpm with a magnetic stir bar and bubbled with Ar at 20 sccm. The gas products were analyzed by an online gas chromatography (GC9720Plus, FULI Instruments) equipment with a thermal conductivity detector (TCD) for H_2 detection.

The electrosynthesis of cyclohexanone oxime tests was performed using the same method as the NO_3RR , except using different electrolytes. For the electrosynthesis of cyclohexanone oxime from NO_3^- , the electrolyte used Ar-protected 1.0 M KOH + 1.0 M KNO₃ with CYC. For the electrosynthesis of cyclohexanone oxime from NO_2^- , the electrolyte was Ar-protected 1.0 M KOH + 1.0 M KNO₂ + 40 mM CYC. KNO₃ (99%) and KNO₂ (97%) were from Alfa Aesar. Cyclohexanone (AR, 99.5%) was from Aladdin, cyclohexanone oxime (> 98%) was from D&B and cyclohexylamine (standard for GC, > 99.5%) was from Macklin.

The prolonged conversion test for the electrosynthesis of cyclohexanone oxime by ZnPc MDE(H) was conducted in a commercial flow cell from Gaoss Union (Supplementary Fig. 26). This device was divided into three parts by a gas diffusion electrode (GDE) and a bipolar membrane (Fumasep FBM-PK). The window area for electrolysis was set to $2 \times 2 \, \text{cm}^2$. The GDE working electrodes of ZnPc MDE(H) were prepared by drop-casting catalyst ink onto a $3 \times 3 \, \text{cm}^2$ carbon fiber paper (29BC, SGL Carbon), giving a catalyst mass loading of 0.4 mg cm 2 . The counter electrode was a nickel foam plate (0.5 mm, YLS), and the reference electrode was an Ag/AgCl electrode (3.0 M KCl, Gaoss Union). The cathode electrolyte was $1.0 \, \text{M}$ KOH + $1.0 \, \text{M}$ KNO $_3$ + $40 \, \text{mM}$ CYC, and the anode electrolyte was $1.0 \, \text{M}$ KOH. The electrolytes, both in the anode and cathode compartments, were recycled with a flow rate of $15 \, \text{ml}$ min $^{-1}$. During the process, Ar flowed into the back side of the working electrode at a rate of $5 \, \text{sccm}$.

Error bars in this work were calculated by averaging three independent measurements.

Product quantification

NO₂-, NH₂OH, and NH₃ were quantified using the same colorimetric methods reported in our previous study². The samples used in the colorimetric methods were first neutralized and diluted to suitable concentrations. In NO_2^- quantification, $100\,\mu L$ of a 4-aminobenzenesulfonamide (99.82%, Bide pharma) aqueous solution (10 g L⁻¹ in 10 wt% HCl, Dongjiang Chemical Reagent) was added into 2 mL of the sample and allowed to react for 8 mins; 100 µL of a N-(1naphthyl) ethylenediamine dihydrochloride (98%, Aladdin) aqueous solution (1 g L-1) was subsequently added and allowed to further react for 10 mins. In NH₃ quantification, 500 μL of an aqueous solution containing 0.4 M sodium salicylate (AR, ≥ 99.5%, General-Reagent from Titan Co. Ltd) and 0.32 M sodium hydroxide (ACS, ≥ 98%, General-Reagent), 50 µL of a sodium hypochlorite aqueous solution containing ~4.5% active chlorine (Aladdin) and 0.75 M sodium hydroxide, and 50 μL of a sodium nitroferricyanide (III) dihydrate (ACS, ≥ 99%, Sigma-Aldrich) aqueous solution (10 mg mL⁻¹) were sequentially added to 3 mL of the sample. For the quantification of NH₂OH, 100 μL of an aqueous acetate buffer (1.0 M sodium acetate (99%, J&K) + 1.0 M acetic acid (≥ 99.5%, Xilong Scientific)), 100 µL of a 4 mM ammonium ferric sulfate (98%, Macklin) aqueous solution and 100 µL of a 10 mM 1, 10phenanthroline (98.74%, Bide pharma) ethanolic solution were sequentially added into 3 mL of the sample. The organic products (cyclohexanone and cyclohexanone oxime) were quantified by ¹H NMR (Supplementary Fig. 19), where 10 mM potassium benzoate (99%, Alfa Aesar) in 100 μl of D₂O (99.8 atom%, Acros) was used as the internal standard.

NH₂OH was also quantified using the reported NMR method with a slight modification²⁵. 10 μ l of cyclohexanone was injected into 2 mL electrolyte after electrocatalysis and stirred vigorously for 1 minute. 100 μ l of electrolyte, 300 μ l of deionized water and 100 μ l of D₂O with 10 mM potassium benzoate reference were mixed, and the ¹H-NMR was used to take the NMR test.

Computational details

The first-principle calculations were based on the spin-polarized DFT calculations using the Vienna Ab initio Simulation Package (VASP), similar to those reported in our previous study 37 . The projector augmented wave (PAW) potentials 38 for the core and the revised Perdew –Burke–Ernzerhof (rPBE) $^{39-41}$ for the exchange-correlation functional were used, as rPBE improves the chemisorption energetics of atoms and molecules on transition-metal surfaces 41 . The cutoff energy was 500 eV for the valence electrons. The structures were all optimized until the force on each atom was less than 0.01 eV Å $^{-1}$, and the energy tolerance was less than 10^{-5} eV on each atom. The cluster models for MPcs were placed in a box of size $24\times24\times15$ Å. The implicit solvent model was applied for the solvent correction by using VASPsol 42,43 .

In-situ ATR-FTIR spectroscopy measurement

The working electrode was prepared by dropping the ZnPc MDE catalyst ink onto the gold-plated Si prismatic window of the Nicolet iS50 FTIR spectrometer (Thermo Fisher). The Pt wire and Ag/AgCl electrodes were used as the counter and reference electrodes, respectively (Supplementary Fig. 27). The Ar-protected 1.0 M KOH + 1.0 M KNO $_3$ solution was employed as the electrolyte. Spectra were recorded at an interval of 0.03 V with a continuous change in applied potential from 0 V to –2.5 V vs. Ag/AgCl. The background spectrum of the catalyst was acquired at an open-circuit voltage before the electrochemical test.

In-situ DEMS measurement

In the in-situ DEMS experiment, a mass spectrometry (QAS 100, Linglu instruments) was connected to the electrochemical cell via a condenser, and gas products were conducted to the mass spectrometry through a porous PTFE membrane (Porosity $\geq 50\%$, pore size ≤ 20 nm, Linglu instruments) coated on the back side of the working electrode (Supplementary Fig. 28). The working electrode was prepared by loading the ZnPc MDE ink on the 29BC carbon paper (0.2 mg cm $^{-2}$, 1 cm $^{-2}$). Pt wire and Ag/AgCl electrodes were used as counter and reference electrodes, respectively. The electrolyte was 50 mL Arprotected 1.0 M KOH + 1.0 M KNO $_3$ (14 N or 15 N) solution. In the multipotential steps experiment, potentiostatic tests at -0.70 V vs. RHE were conducted and the measurement was ended after 4 cycles. In the LSV test, the applied potential was scanned from 0 V to -0.80 V vs. RHE, with a scanning rate of 1.0 mV s $^{-1}$.

Data availability

The authors declare that the main data supporting the findings of this study are available within the article and its Supplementary Information. Extra data are available from the corresponding authors upon request. Source data are provided with this paper.

References

- Huang, JiananE. et al. CO₂ electrolysis to multicarbon products in strong acid. Science 372, 1074–1078 (2021).
- Wu, Y., Jiang, Z., Lin, Z., Liang, Y. & Wang, H. Direct electrosynthesis of methylamine from carbon dioxide and nitrate. *Nat. Sustain.* 4, 725–730 (2021).
- Tao, Z., Rooney, C. L., Liang, Y. & Wang, H. Accessing organonitrogen compounds via C-N coupling in electrocatalytic CO₂ reduction. *J. Am. Chem. Soc.* 143, 19630–19642 (2021).
- Wu, Y. et al. Electrosynthesis of a nylon-6 precursor from cyclohexanone and nitrite under ambient conditions. *Nat. Commun.* 14, 3057 (2023).
- Wu, Y. et al. Electrocatalytic synthesis of nylon-6 precursor at almost 100 % yield. Angew. Chem. Int. Ed. 62, e202305491 (2023).
- Lewis Richard, J. et al. Highly efficient catalytic production of oximes from ketones using in situ-generated H₂O₂. Science 376, 615–620 (2022).

- Luo, Y. et al. Selective electrochemical synthesis of urea from nitrate and CO₂ via relay catalysis on hybrid catalysts. *Nat. Catal.* 6, 939–948 (2023).
- 8. Xie, M. et al. Intermetallic single-atom alloy In–Pd bimetallene for neutral electrosynthesis of ammonia from nitrate. *J. Am. Chem. Soc.* **145**, 13957–13967 (2023).
- Zhou, Y. et al. Long-chain hydrocarbons by CO₂ electroreduction using polarized nickel catalysts. Nat. Catal. 5, 545–554 (2022).
- Chen, F.-Y. et al. Efficient conversion of low-concentration nitrate sources into ammonia on a Ru-dispersed Cu nanowire electrocatalyst. Nat. Nanotechnol. 17, 759–767 (2022).
- Jiang, Z. et al. Molecular electrocatalysts for rapid and selective reduction of nitrogenous waste to ammonia. Energy Environ. Sci. 16, 2239–2246 (2023).
- Xu, H., Ma, Y., Chen, J., Zhang, W.-x & Yang, J. Electrocatalytic reduction of nitrate – a step towards a sustainable nitrogen cycle. Chem. Soc. Rev. 51, 2710–2758 (2022).
- Zhang, X. et al. Recent advances in electrocatalytic nitrite reduction. Chem. Commun. 58, 2777–2787 (2022).
- Zhang, X. et al. Recent advances in non-noble metal electrocatalysts for nitrate reduction. Chem. Eng. J. 403, 126269 (2021).
- 15. Krzywda, P. M. et al. Electroreduction of NO₃⁻ on tubular porous Ti electrodes. *Catal. Sci. Technol.* **12**, 3281–3288 (2022).
- 16. Zhang, J. et al. Molecular tuning for electrochemical CO_2 reduction. Joule **7**, 1700–1744 (2023).
- Buuml, Chel K. H., Moretto H.-H., Werner D. Industrial Inorganic Chemistry, 1. Aufl. edn. Wiley-VCH (2008).
- Adarakatti, P. S., Crapnell, R. D. & Banks, C. E. Electroanalytical overview: the sensing of hydroxylamine. *Anal. Methods* 15, 2709–2720 (2023).
- Semon, W. L. The preparation of hydroxylamine hydrochloride and acetoxime. J. Am. Chem. Soc. 45, 188–190 (1923).
- Driessen, R. T. et al. Industrial process design for the production of aniline by direct amination. *Chem. Eng. Technol.* 40, 838–846 (2017)
- 21. Chen, R. et al. Continuous NO upcycling into ammonia promoted by SO₂ in flue gas: poison can be a gift. *Environ. Sci. Technol.* **57**, 12127–12134 (2023).
- Pérez-Gallent, E., Figueiredo, M. C., Katsounaros, I. & Koper, M. T. M. Electrocatalytic reduction of nitrate on copper single crystals in acidic and alkaline solutions. *Electrochim. Acta* 227, 77–84 (2017).
- Shen, J., Birdja, Y. Y. & Koper, M. T. M. Electrocatalytic nitrate reduction by a cobalt protoporphyrin immobilized on a pyrolytic graphite electrode. *Langmuir* 31, 8495–8501 (2015).
- 24. García, M. et al. Nitrite reduction on a multimetallic porphyrin/polyoxotungstate layer-by-layer modified electrodes. *Electrochim.* Acta **192**, 61–71 (2016).
- 25. Zhou, J. et al. Linear adsorption enables NO selective electroreduction to hydroxylamine on single Co sites. *Angew. Chem. Int. Ed.* **62**, e202305184 (2023).
- Bari, S. E., Amorebieta, V. T., Gutiérrez, M. M., Olabe, J. A. & Doctorovich, F. Disproportionation of hydroxylamine by water-soluble iron(III) porphyrinate compounds. *J. Inorg. Biochem.* 104, 30–36 (2010).
- 27. Wu, Y., Jiang, Z., Lu, X., Liang, Y. & Wang, H. Domino electro-reduction of $\rm CO_2$ to methanol on a molecular catalyst. *Nature* **575**, 639–642 (2019).
- 28. Yuan, Y. et al. Deciphering the selectivity descriptors of heterogeneous metal phthalocyanine electrocatalysts for hydrogen peroxide production. *Chem. Sci.* **13**, 11260–11265 (2022).
- 29. Lin, Z. et al. Cobalt- N_4 macrocyclic complexes for heterogeneous electrocatalysis of the CO_2 reduction reaction. *Chin. J. Catal.* **43**, 104–109 (2022).

- Fortune, W. B. & Mellon, M. G. Determination of iron with o-phenanthroline: a spectrophotometric study. *Ind. Eng. Chem. Anal. Ed.* 10, 60–64 (1938).
- 31. Kong, X. D. et al. Coordinate activation in heterogeneous carbon dioxide reduction on Co-based molecular catalysts. *Appl. Catal. B-Environ.* **268**, 118452 (2020).
- Fang, J.-Y. et al. Ampere-level current density ammonia electrochemical synthesis using CuCo nanosheets simulating nitrite reductase bifunctional nature. Nat. Commun. 13, 7899 (2022).
- 33. Li, M. et al. Electrosynthesis of amino acids from NO and α -keto acids using two decoupled flow reactors. *Nat. Catal.* **6**, 906–915 (2023).
- Matsui, T. et al. In situ attenuated total reflection infrared spectroscopy on electrochemical ammonia oxidation over Pt electrode in alkaline aqueous solutions. *Langmuir* 31, 11717–11723 (2015).
- Wu, J. et al. Integrated tandem electrochemical-chemical electrochemical coupling of biomass and nitrate to sustainable alanine. Angew. Chem. Int. Ed. 62, e202311196 (2023).
- Heenan, A. R., Hamonnet, J. & Marshall, A. T. Why careful iR compensation and reporting of electrode potentials are critical for the CO₂ reduction reaction. ACS Energy Lett. 7, 2357–2361 (2022).
- 37. Kresse, G. & Furthmüller, J. Efficient iterative schemes for ab initio total-energy calculations using a plane-wave basis set. *Phys. Rev. B* **54**, 11169–11186 (1996).
- Kresse, G. & Joubert, D. From ultrasoft pseudopotentials to the projector augmented-wave method. *Phys. Rev. B* 59, 1758–1775 (1999).
- 39. Perdew, J. P., Burke, K. & Ernzerhof, M. Generalized gradient approximation made simple. *Phys. Rev. Lett.* **77**, 3865–3868 (1996).
- 40. Perdew, J. P., Ernzerhof, M. & Burke, K. Rationale for mixing exact exchange with density functional approximations. *J. Chem. Phys.* **105**, 9982–9985 (1996).
- Hammer, B., Hansen, L. B. & Nørskov, J. K. Improved adsorption energetics within density-functional theory using revised Perdew-Burke-Ernzerhof functionals. *Phys. Rev. B* 59, 7413–7421 (1999).
- Mathew, K. et al. Implicit solvation model for density-functional study of nanocrystal surfaces and reaction pathways. J. Chem. Phys. 140, 084106 (2014).
- 43. Mathew, K. et al. Implicit self-consistent electrolyte model in planewave density-functional theory. *J. Chem. Phys.* **151**, 234101 (2019).

Y.L. acknowledges financial supports from National Natural Science

Acknowledgements

foundation of China (22075125, Y.L.), Guangdong - Hong Kong - Macao Joint Laboratory Fund (2019B121205001, Y.L.), and Shenzhen fundamental research funding (JCYJ20220530114607017, JCYJ20220818100618039, Y.L.). X.Z. acknowledges financial supports from National Key Research and Development Project (2023YFC3710800, X.Z.) and Zhejiang Provincial Natural Science Foundation of China (LDT23E06012E06, X.Z.). The computational resource is supported from the Center for Computational Science and Engineering (SUSTech). The authors sincerely thank Dr. Weiwei Yang (State Key Laboratory of Clean Energy Utilization Instrumental Analysis Center) for her kind help in performing In-situ FTIR and DEMS.

Author contributions

Y.T., Z.J. and Y.Y. contributed equally to this work. Y.L. conceived the project and designed the experiments. Y.T. and Z.J. carried out the preparation, characterization and electrochemical measurements of the catalysts. Y.Y. performed the DFT calculation. Y.T. and Z.L. validated the availability of the NH₂OH quantification methods. X.G., X.Z., J.D., L.X., C.J., Y.T. and Z.J. carried out the in-situ ATR-FTIR and in-situ DEMS characterizations. Y.T., Z.J. and J.Z. carried out the electron microscopy characterizations. Y.T., Z.J., B.C. and Y.L. prepared the figures. Y.L., Z.J., X.G. and Y.T. analyzed the data and wrote the manuscript with input from all authors. All authors discussed the results and commented on the manuscript.

Competing interests

The authors declare no competing interests.

Additional information

Supplementary information The online version contains supplementary material available at https://doi.org/10.1038/s41467-024-54204-2.

Correspondence and requests for materials should be addressed to Zhan Jiang, Xiao Zhang, Xiang Gao or Yongye Liang.

Peer review information *Nature Communications* thanks Rachel Baker, and the other, anonymous, reviewers for their contribution to the peer review of this work. A peer review file is available.

Reprints and permissions information is available at http://www.nature.com/reprints

Publisher's note Springer Nature remains neutral with regard to jurisdictional claims in published maps and institutional affiliations.

Open Access This article is licensed under a Creative Commons Attribution-NonCommercial-NoDerivatives 4.0 International License, which permits any non-commercial use, sharing, distribution and reproduction in any medium or format, as long as you give appropriate credit to the original author(s) and the source, provide a link to the Creative Commons licence, and indicate if you modified the licensed material. You do not have permission under this licence to share adapted material derived from this article or parts of it. The images or other third party material in this article are included in the article's Creative Commons licence, unless indicated otherwise in a credit line to the material. If material is not included in the article's Creative Commons licence and your intended use is not permitted by statutory regulation or exceeds the permitted use, you will need to obtain permission directly from the copyright holder. To view a copy of this licence, visit https://creativecommons.org/licenses/by-nc-nd/4.0/.

© The Author(s) 2024